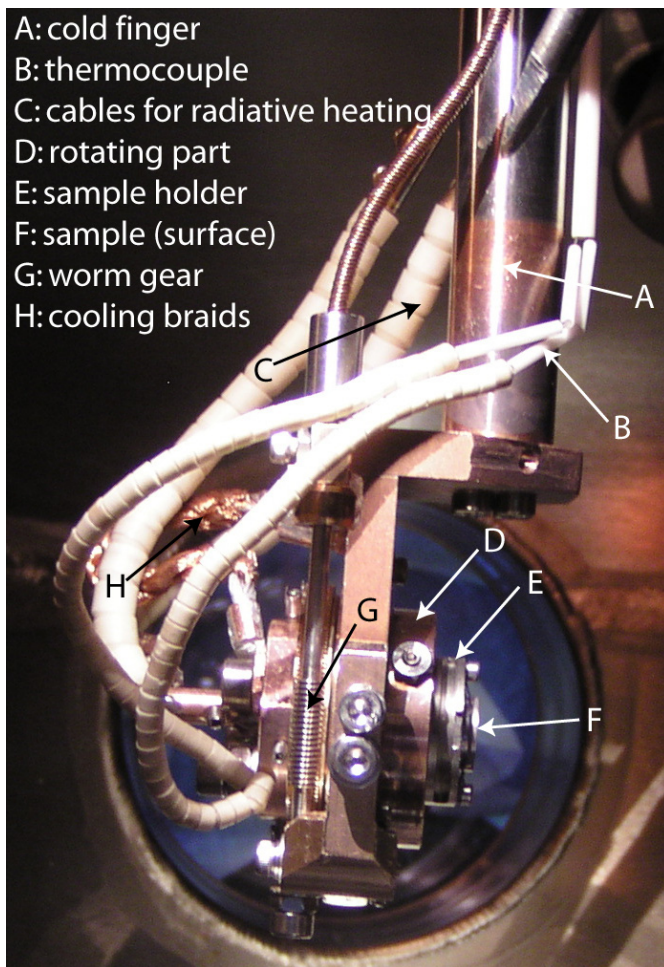# 2 Experimental

2.1.1 Ultra high vacuum equipment

The growth of metal layers on substrates is very sensitive to contamination of the substrate, therefore it is essential that growth and characterization are performed under ultra high vacuum conditions. All the experiments reported here have been performed in the same ultra high vacuum (UHV) chamber with a base pressure of $2x10^{-10}$ mbar or better. This pressure was reached with the standard use of turbo-, ion- and titanium sublimation pumps, and baking the chamber at a temperature of 130°C for at least 36 hours. The chamber is equipped with a number of preparation and analysis tools. The primary analysis tool is the Phoibos 100 electron energy analyser equipped with channelplate detection and CCD camera (Specs GmbH, Berlin); more about this analyser will follow in Section 2.1.3. As a secondary analysis tool, low energy electron diffraction (LEED) was used in order to determine the crystalline symmetry of the arrangement of the atoms.

For the evaporation of the metals, a home-made water cooled molecular beam epitaxy (MBE) cell was used, where the temperature of the cell was controlled through the use of a PID controller with a 0-5 V output (West Inc.) in combination with a programmable power supply (Delta electronics). This way a stable evaporation rate was reached, which was reproducible over large time intervals.

Crucial for the experiments was the development of a sample manipulator. The design criteria were: (1) that the sample should be transferable without breaking the vacuum of the chamber, (2) that it could be cooled to temperatures low enough to suppress the high mobility of the metal atoms, (3) that it could be heated to very high temperatures in different ways, depending on the type of sample used, in order to clean the sample, and (4) that it could be manipulated with at least five degrees of freedom.

These are: the three perpendicular lateral movements (x, y, z), a rotation of the sample around an axis parallel to the surface, the so-called polar angle (θ), and a rotation around the surface normal, the so-called azimuthal angle (φ). In order to satisfy these demands, the latest design iteration features a round sample holder that can be transferred by screwing it on or off the manipulator. The inside of the cylinder is conical in order to optimise the contact area with the manipulator for effective cooling. The combination of the screwing and conical design makes the sample holder self-centering during transfer. This makes the act of changing samples from the load lock to ultra

A: cold finger
B: thermocouple
C: cables for radiative heating
D: rotating part
E: sample holder
F: sample (surface)
G: worm gear
H: cooling braids

Figure 2.1: Photograph of the bottom part of the manipulator used in the experiments described in this work. The surface of the sample faces to the right in this image. The letters A - H indicate some of the essential parts of the manipulator head.

high vacuum only a matter of minutes. The sample holder is positioned on a part of the manipulator that can be rotated in a ball bearing through a worm gear with a rotary feedthrough outside of UHV, thereby providing the azimuthal rotation of the sample. Figure 2.1 shows a photograph of the sample holder part of the resulting manipulator, where all the relevant components are indicated. The other four degrees of freedom were already commercially supplied by the manufacturer of the manipulator (Thermionics Inc.).

The sample was cooled by use of a liquid nitrogen or helium cold finger. In order to optimise the heat transfer from the sample, oxygen free high conductivity copper was used to construct the individual parts of the manipulator. The heat transfer across the ball bearing was accomplished by using flexible braids of the same material. With this construction a temperature of 88 Kelvin on the sample could be reached when cooling with liquid nitrogen. In order to control the warming up of the sample, a filament was located in the rotating part on which the sample holder is mounted. Through radiative heating, the sample holder could be warmed up, and by applying a high voltage between the sample holder and filament it could be used for e-beam heating. Most semiconductors can, however, be more evenly heated by applying a current through them, referred to as direct current heating. Because the whole manipulator was isolated from ground when not measuring, and one half of the sample holder was only connected to the manipulator through the sample, a current could be passed through the sample by connecting this part to ground with a wobble stick and then applying a current from manipulator to ground.

The next step in manipulator design and optimization is controlling all the lateral motions and the angles with stepper motors. These motors are themselves controlled by the computer in order to synchronise the data acquisition and sample motion.

2.1.2 Angle Resolved Photoemission Spectroscopy

Most physical properties of solids are characterized by the electron distribution close to the Fermi level; therefore an effective way to determine the physical origin of these properties would be a complete measurement of the electron distribution around the Fermi level. For measurements of the occupied states, a standard tool nowadays is angle resolved photoemission spectroscopy (ARPES). Photoemission spectroscopy is based on the photoelectric effect, in which an electron may be emitted from a surface when it is illuminated. Experiments on sparking phenomena in 1887 lead to the first observation of this effect by Hertz[1], and in 1905 Einstein explained the effect as a quantum phenomenon[2] based on the concept of the photon as a particle of light. The general principle is that an electron in an occupied state in the solid can be optically excited by a photon into an unoccupied state. When the energy of the photon hv is larger than the sample work function Φ, some of the electrons will be able to escape the solid and can be detected. The principle and experimental setup for ARPES is schematically depicted in Figure 2.2. A collimated monochromatic beam of photons hits upon the sample, thereby causing the emission of electrons. The energy and emission angle of the electrons can be detected with an electron energy
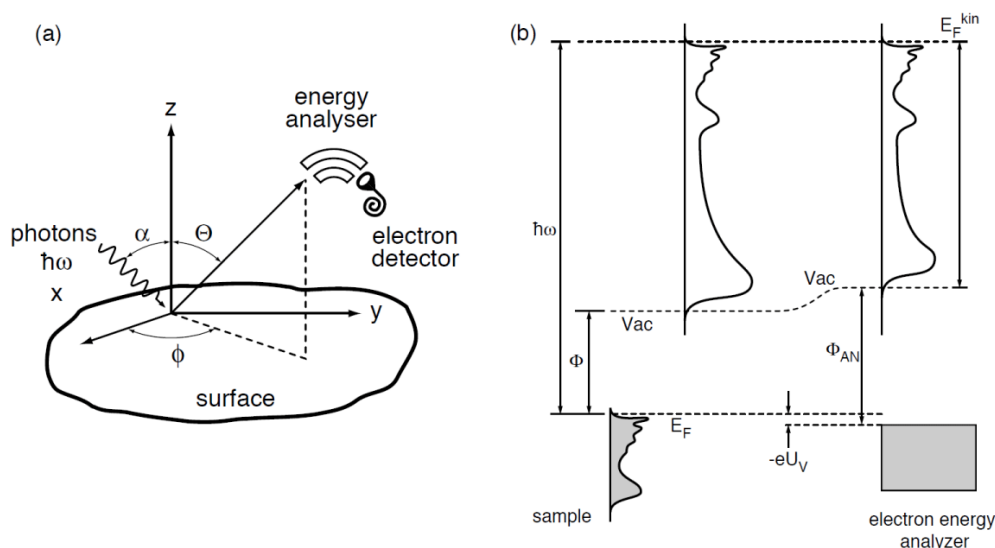

Figure 2.2: Schematics of the angle resolved photoemission spectroscopy geometry (a) and principle (b). Φ and Φ_{AN} are the work function of the sample and the analyser, respectively. Also a possible bias voltage $-eU_V$ is indicated.

---

1   H. Hertz, Annalen der Physik und Chemie, **31**, 983 (1887)
2   A. Einstein, Annalen der Physik, **17**, 132 (1905)

analyser. Scanning the detected kinetic energy while keeping the photon energy constant will give information about the density of states (DOS) in the sample. Such a scan is commonly referred to as an electron distribution curve (EDC).

The semi-classical three-step model for the photoemission process provides a good starting ground for most experimental observations; in order to explain more complex processes such as electron-electron and electron-phonon coupling, the full quantum mechanical approach is needed. This is beyond the scope of this introduction, but will be highlighted in Chapter 5 concerning interaction effects in quantum well states. The three-step model divides the photoemission process into three consecutive events: first the excitation of the electron by the photon, secondly the transport of the electron through the material to the surface, and third the escape of the electron through the surface potential barrier.

The photon responsible for the optical excitation of the electron from an occupied to an unoccupied state within the crystal has a negligible momentum, especially in the ultraviolet energy range relevant for this thesis. Therefore the crystal momentum $\hbar \boldsymbol{k}$ is conserved via the exchange of a reciprocal lattice momentum vector $\hbar \boldsymbol{G}$ between the electron and the periodic lattice, resulting in the following momentum conservation rule:

$$\mathbf{k}_f = \mathbf{k}_i + \mathbf{G}, \tag{2.1}$$

where the subscripts f and i refer to the final and initial conditions of the electron. Energy conservation requires that

$$E(\mathbf{k}_f) = E(\mathbf{k}_i) + \hbar \nu . \tag{2.2}$$

In the reduced Brillouin zone scheme, this means that the transition is vertical and can only take place where the energy difference between the initial and final bands is equal to $\hbar \nu$. The next step is the transport of the excited electron through the crystal. The information carried by the electron will not be distorted as long as it does not undergo any scattering events with other electrons, because in these scattering events the energy and direction of the electron can be severely altered. The average distance over which the electron can travel without losing its phase and energy information is called the electron mean free path λ. The maximum escape depth for useful photoelectrons will not be larger than the mean free path of this electron. In order to obtain a feeling for the depth probed by photoemission, consider Figure 2.3, which depicts λ as a function of the kinetic energy of the electron for a wide variety of materials. The general curve does not depend much on the type of material and can therefore be used as a general rule of thumb. For the research presented in this thesis, the kinetic energy of the electrons is around 20 eV, which corresponds to the minimum
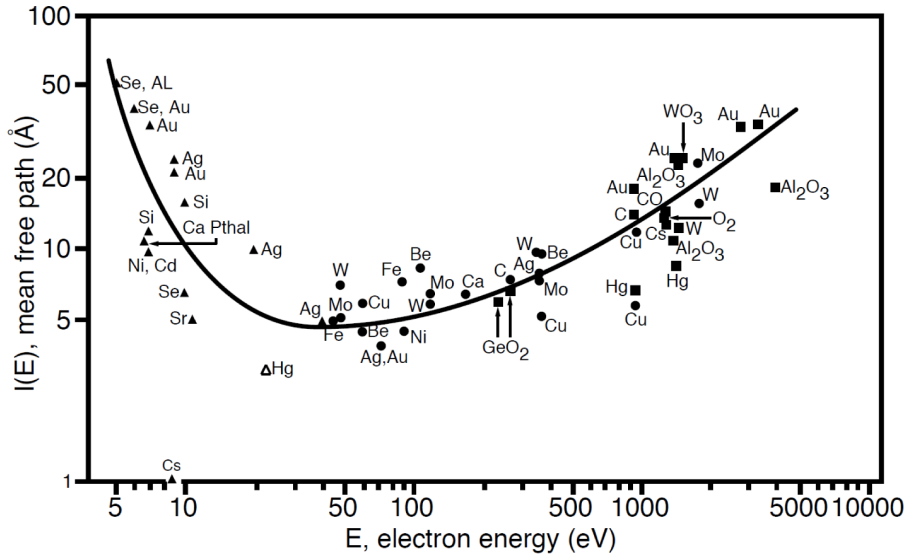
Figure 2.3: Mean free path vs. kinetic energy of the electron, measured for several materials. The minimum is located at approximately 20 eV, corresponding to the kinetic energy used for the experiments presented in this work.

in the electron mean free path. Therefore only the electrons from the topmost few monolayers will contribute to the signal, making ARPES a surface sensitive tool. Due to scattering, a typical EDC will consist of sharp lines from the electrons that reached the surface without any inelastic scattering events, and a structureless background that increases in intensity towards lower binding energies, from the electrons that have experienced single or multiple scattering events.

The third step is the escape of the photoelectron through the surface. If the surface is assumed to be locally flat, which is a very good approximation for the surfaces studied here, the electron wave vector component parallel to the surface $k_{f\parallel}$ will be conserved to within a surface reciprocal lattice vector $g_\parallel$. For an unreconstructed surface this will be equal to the surface parallel component of the bulk reciprocal lattice vector G. The surface parallel wave vector of the electron outside the crystal, $q_\parallel$, is then defined as:

$$\mathbf{q}_\parallel = \mathbf{k}_{f\parallel} + \mathbf{g}_\parallel. \tag{2.3}$$

In the direction perpendicular to the surface, the symmetry of the crystal potential is broken, therefore the electron wave vector in this direction $\mathbf{k}_\perp$ is not conserved when the electron escapes into the vacuum. This is the reason that information about this part of the electron wave vector cannot be directly deduced from the photoemission spectrum.

Once the electron has escaped the crystal, it can be regarded as a free electron and the following dispersion relation is valid

$$E_k = E(\mathbf{k}_f) - E_V = \frac{\hbar^2 \mathbf{q}^2}{2m}, \tag{2.4}$$

where m is the mass of the electron and E_V is the vacuum potential, which can be obtained from the low energy cutoff of the secondary electrons. Using this expression and Equations 2.1 and 2.3, the initial parallel electron wave vector $\boldsymbol{k}_{\|i}$ can be determined as

$$\mathbf{k}_{\|i} = \sqrt{\frac{2mE_k}{\hbar^2}} \sin\theta \, \frac{\mathbf{q}_\|}{|\mathbf{q}_\||} - \mathbf{G}_\| - \mathbf{g}_\| . \qquad (2.5)$$

For an unreconstructed surface, as is the case for the surfaces of the metal overlayers in this work, and by filling in all the relevant constants and knowing the direction of measurement, Equation 2.5 can be simplified into the much more compact formula

$$k_{\|i} \cong 0.52 \sqrt{E_k} \, \sin\theta \, , \qquad (2.6)$$

where the vector notation is replaced by a scalar. Whenever $k_\|$ values are presented in this work, they are derived from this last expression. From energy conservation (Equations 2.2 and 2.4) it is possible to derive an equation for the initial energy of the electron before excitation

$$- E_b = E(\mathbf{k}_i) - E_F = E_k + \Phi - \hbar\nu \qquad (2.7)$$

where the $\Phi = E_V - E_f$ is the work function, E_F is the Fermi energy and E_b is defined as the binding energy of the electron, which is positive for the occupied states and negative for the unoccupied states. From the above set of equations it is clear that for a certain photon energy and known work function, only the kinetic energy and the exit angle of the electron need to be determined to measure the bandstructure in the direction parallel to the surface. How these two quantities can be measured simultaneously will be explained in the next section.

2.1.3 The Omicron AR65 and Specs Phoibos 100 CCD electron energy analysers

The experiments presented in this thesis were performed with two different electron energy analysers. Almost all data for Pb on Cu(111) has been recorded with an AR65 (Omicron GmbH, Taunusstein). This analyser is mounted on a goniometer in order to change the detection angle with respect to the sample normal. At a set angle, three channeltrons record the number of electrons as a function of their kinetic energy, yielding an energy distribution curve. This can then be repeated for different angles in order to measure a full bandstructure. This procedure is tedious and relatively slow. More importantly, the angular acceptance of the analyser is on the order of 1 to 3 degrees, which will limit the final angular resolution of the data. A major advantage of this type of analyser is its simplicity; an electron that travels in the direction of the channeltron will give a number of counts only dependent on the multiplication factor and there is no need for complex electron optics.

All other data was recorded with a Phoibos 100 hemispherical analyser (SPECS GmbH) with a channelplate and charge coupled device (CCD) camera readout, which allows for the simultaneous measurement of the kinetic energy of the electron and its emission angle within a wide angular range. Here it should be noted that I had the pleasure to be the first person, apart from the development team, to work with this analyser and to explore its full capabilities. As a result of this, the analyser and peripheral equipment became part of an ongoing development project.
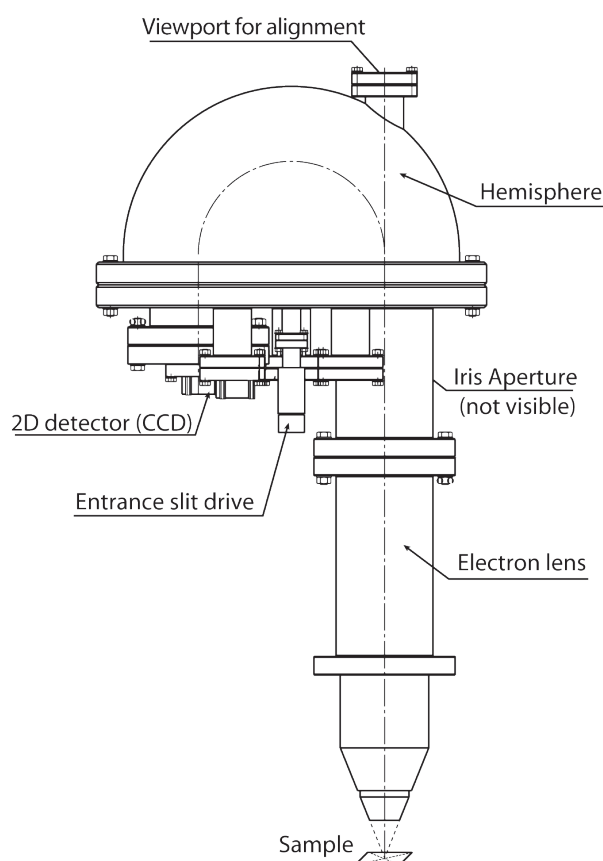

Figure 2.4: Drawing of the Phoibos 100 electron energy analyser with image detector. The most essential parts are indicated in the drawing. In the experiment the analyser is mounted horizontally.

In order to obtain a better understanding of the data recorded with this analyser, it is useful to start by considering a cross-section sketch of the analyser as depicted in Figure 2.4. Three separate parts of the analyser can be distinguished: first, the lens system, secondly, the hemispheres and finally the 2D detector (not clear in the image). A photoemitted electron from the sample will first travel through the lens system, and electron optical settings (the so-called lens modes) will determine the exact path of the electron. Two different types of lens modes can be distinguished: the spatial and the angular resolving modes. The spatial resolving modes will map electrons escaping from different parts of the sample at different positions in the image plane. This is especially useful to obtain high count rates for core level photoemission, or to align the photon beam on the sample, depending on the exact settings. This group of lens modes was not used in this work to gather experimental data, but only to check the alignment of the photon beam on the sample with respect to the focus of the analyser. A description of the procedure followed in order to obtain a good alignment of the sample and analyser will be given in Section 2.1.4.
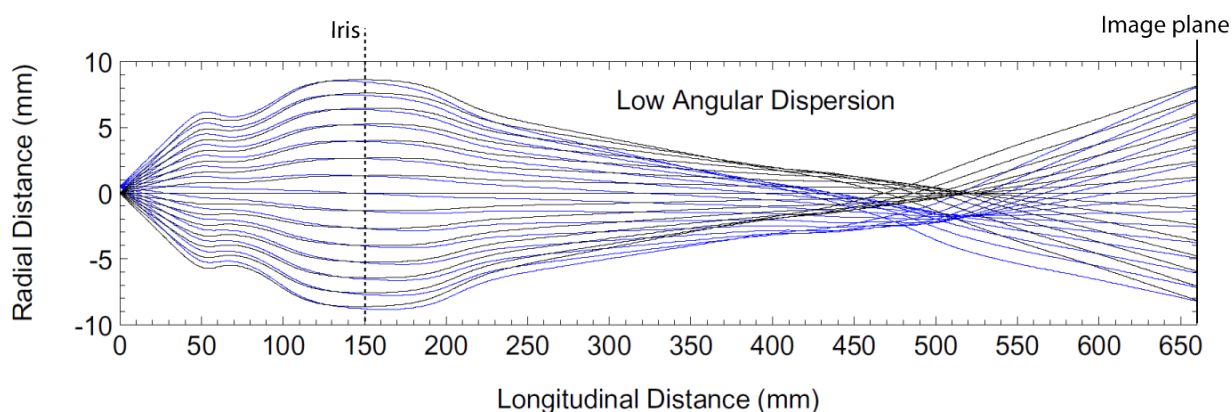

Figure 2.5: Calculated electron trajectories through the analyser for two spatially separated origins at the sample. The sample surface is located at 0 mm, the iris at 150 mm, the hemispherical part starts at 350 mm, and at 660 mm the electrons are imaged. The trajectories are perpendicular to the drawing in Figure 2.4.

As the name implies, the angle-resolved lens modes are best suited for angle-resolved photoemission spectroscopy. Three different angle resolved lens modes are available that are different only in the angular acceptance region: Medium Angular Dispersion (MAD) for ±4°, Low Angular Dispersion (LAD) for ±7° and the Wide Angle Mode (WAM) for ±13°. Except for some ultra-high angular resolution data for which MAD was used, most data was recorded using the LAD lens mode. Figure 2.5 shows the calculated electron trajectories for the LAD lens mode with the zero point corresponding to the sample surface; the radial distance depicted is perpendicular to the cross section in Figure 2.4, and to the curvature of the hemispheres. Trajectories are depicted for two sets of electrons originating 0.5 mm apart, and for every degree up to ±7°. It can be seen that electrons originating from different parts of the sample but with the same emission angle are mapped at the

same position of the image plane, whereas electrons with different emission angles are separated at the image plane. Around 150 mm away from the sample, an iris can be closed in order to block electrons that originate from any distance away from the radial axis, therefore decreasing the acceptance area and suppressing any stray electrons. At the same time, however, the angular acceptance is decreased, such that one has to find an optimum between these two factors.

When the electrons arrive at the hemispherical part of the analyser, their pathway in the direction perpendicular to Figure 2.4 remains unaffected and this part of the analyser does therefore not change the angular distribution of the electrons. Due to the electric field between the hemispheres, electrons with different kinetic energies will be spatially separated from each other; electrons with a higher velocity will arrive furthest away from the centre of the sphere. The energy resolution of a 180° hemispherical electron energy analyser is determined by the entrance and exit slits (s_1 and s_2 respectively), the radius of the sphere R_0, and by the pass energy E_P as follows[3]

$$\Delta E = \frac{s_1 + s_2}{4R_0} E_P + higher\ order\ terms\ . \tag{2.8}$$

For an analyser with CCD detector, the exit slit cannot be varied and can be estimated as the size of the area imaged by one CCD pixel in the energy direction, which is 0.1 mm. This constant, but very small, exit slit is a major advantage of this type of analyser; it will give an optimal energy resolution without lowering the count rate. Another fixed quantity is the radius of the analyser, which is 100 mm. This leaves the entrance slit and the pass energy as the only variables. Typical values for the entrance slit are between 0.1 and 1 mm. In the experiments presented here, useful values for the pass energy are between 5 and 50 eV. For the often used typical values of 0.5 mm for the entrance slit, and 20 eV pass energy, the achieved energy resolution of the analyser is 30 meV. This can be reduced to 2.5 meV, taking realistic experimental considerations of pass energy and entrance slit into account. Besides affecting the energy resolution, the pass energy also determines the energy window that can be recorded for a fixed kinetic energy. Electrons with a energy greater/less than E_k plus/minus 10% of the pass energy will end up outside the acceptance window. Therefore the total energy range of one image is centred at the set kinetic energy and is 20% of E_P.

These electrons, whose exit angles and kinetic energies are spatially separated from each other, will hit the first of two microchannel plates (MCP) in chevron stacking, in order to multiply the signal before hitting a fast phosphorus screen. The image created by the screen is then demagnified seven times with a conventional lens system onto the CCD sensor to produce an image of 640x480 pixels. Such an image is depicted in Figure 2.6 for a 9 monolayer thick indium film on Si(111)7x7, taken at a photon energy of 26 eV in the MAD lens mode. The centre of the image is at a kinetic energy of 20.9 eV and the pass energy is 10 eV, yielding an energy window of 2 eV. The image shows the indium $5p_{x,y}$ QWS at the edge of the surface Brillouin zone, the bright feature in the

---

3   E.H.A. Granneman and M.J. van der Wiel, *Handbook on Synchrotron Radiation*, edited by E. Koch (North-Holland, Amsterdam, 1983), Vol. 1
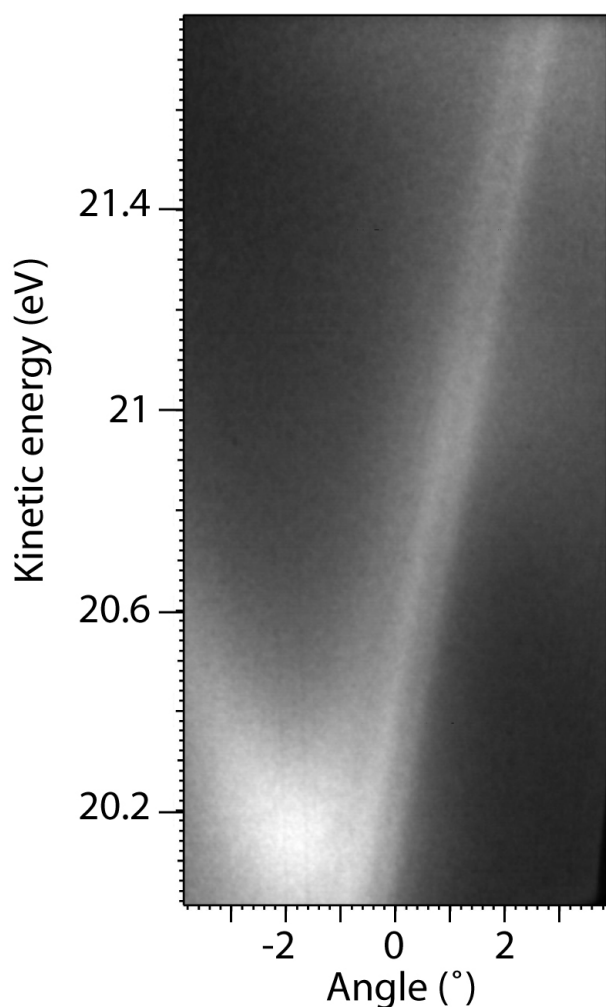
Figure 2.6: Kinetic energy vs. emission angle photoemission image for a 9 ML thick In film on Si(111)7x7. The features are the $5p_{x,y}$ band derived QWS close to the boundary of the SBZ. The image is obtained in the MAD lens mode with a photon energy of 26 eV, and a kinetic energy of 20.9 eV. A measure for the angular resolution can be determined from the spacing of the two diagonal lines, this is less than 0.25°. For a further description of the image see Section 4.4.

lower left corner is due to the same states bending back. In Section 4.4 the full electronic structure of this system is discussed. Two almost vertical very sharp parallel lines can be distinguished, with a third one joining towards the bottom of the image. From the separation of these lines in the horizontal direction, a measured experimental angular resolution better than 0.25° can be concluded, at the used kinetic energy this corresponds to approximately 0.01 Å^{-1}.

The use of MCP has been mentioned as a means to multiply the number of electrons that will hit the screen. The most effective multiplication occurs when two channel plates are positioned in the so-called chevron position, where the tilt of the channels is opposite to each other. This is a well-known technique that is used in many devices; one thing that is hardly ever touched upon is the importance of this alignment for any optical characteristics. A slight misalignment between two regular repeating structures results in the well-known Moiré patterns; relatively small angular misalignment can result in beautiful and complex patterns. Microchannel plates have locally a very regular structure with the rotational symmetry deceasing further away from a set point, and are therefore prone to creating Moiré patterns when stacked. Figure 2.7(a) shows such a pattern, acquired with a homogeneous source of low energy electrons from a heating filament; hence the image has no sharp edges and no clear features. Over the entire image, hexagonal patterns of
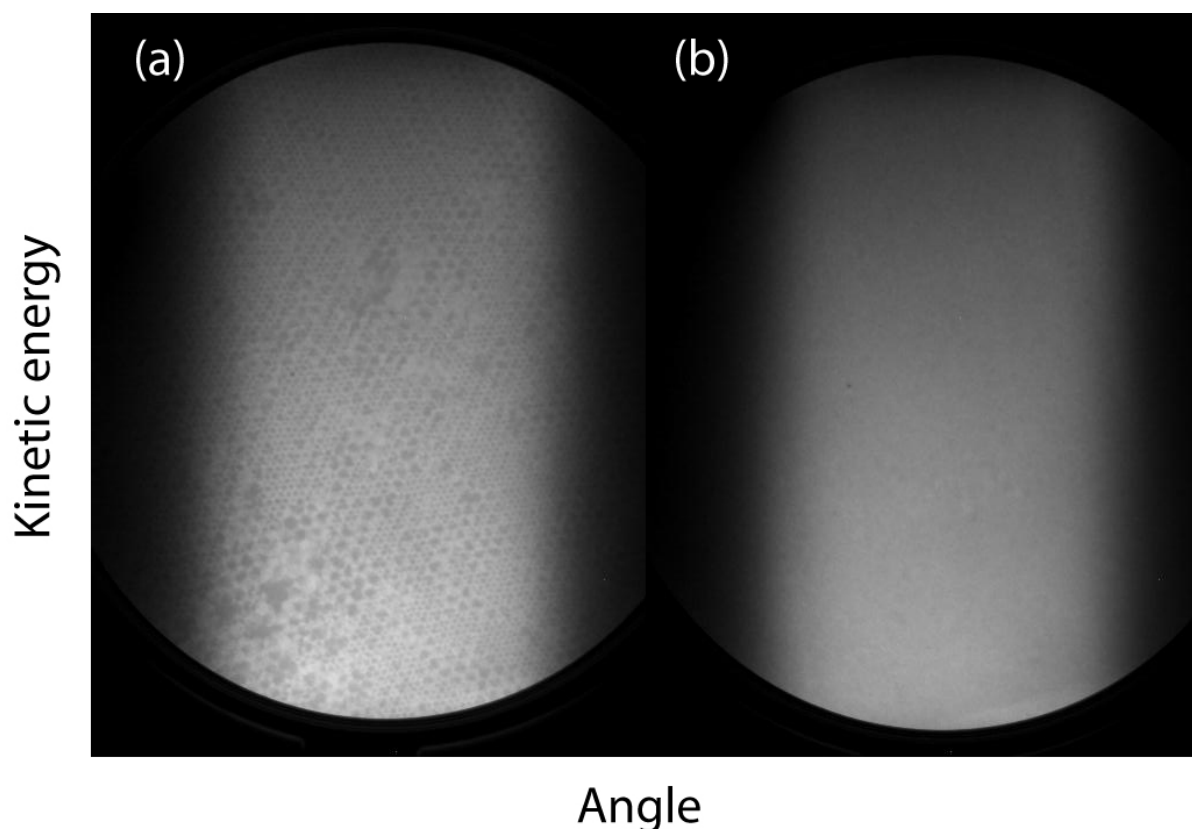
Figure 2.7: CCD images of the MCP obtained with low energy electrons from the heating filament. (a) The MCP are almost perfectly aligned in the chevron stacking, note the strong Moiré pattern. (b) The MCP are intentionally misaligned ~20°, the Moiré pattern is suppressed.

different sizes can be observed, which have all the typical characteristics of a Moiré pattern. One could assume that this is caused by a relatively large misalignment of the two channel plates; however, the truth is a little more complex. Moiré patterns caused by the imperfect alignment of two MCP will show up at angles as small as several milliradians[4], which already requires special micro manipulation tools. The best way to suppress the Moiré pattern is by deliberately introducing a misalignment of around 20° between our set of MCP. For comparison, Figure 2.7(b) shows an image after applying this extreme misalignment and it is easily observed that the Moiré pattern is suppressed.

---

4   A.S. Tremsin *et al*, Applied Optics, **38**, 11, 2240 (1999)

2.1.4 Alignment of Sample, Analyser and Light

The lens of the Phoibos 100 analyser has a well defined focus; i.e. the area of the sample from which the electrons originate that will pass through the lens system. At the focal distance of 40 mm, the size of this area is around 0.5 mm in diameter. The typical focus of a synchrotron light source is between 80 and 300 μm, meaning that this spot should be positioned inside the focal area of the analyser to create a complete overlap. There are three relative positions that have to be optimized in this system; first, between the sample and analyser, secondly, between sample and light source, and last between light source and analyser. These relative positions are intertwined as sketched in Figure 2.8, which makes the positioning even more complex. In the following, the influence of each of the abovementioned relative positions on the final data will be discussed.

When the sample is laterally displaced in front of the analyser, a different part of the sample, or in extreme cases the sample holder, is examined. Assuming a homogeneous sample, this has very little influence on the data quality and is only used to find the centre of the sample. The distance between sample and analyser will influence the angular resolution of the data. Furthermore, when the distance is changed away from 40 mm, the focal area will also increase, which might lead to the appearance of artefacts in the image.

The sample holder has been constructed in such a way that the lateral positions of the surface of the sample will not change when the polar angle is rotated. In other words, the centre of the surface is exactly at the axis of rotation. Consequently, the position of the light spot will not move on the sample when the beam is focussed on the axis of rotation. When this positioning is less perfect, a different part of the sample is imaged every time the sample is rotated, and the distance between the illuminated area and the analyser will change.
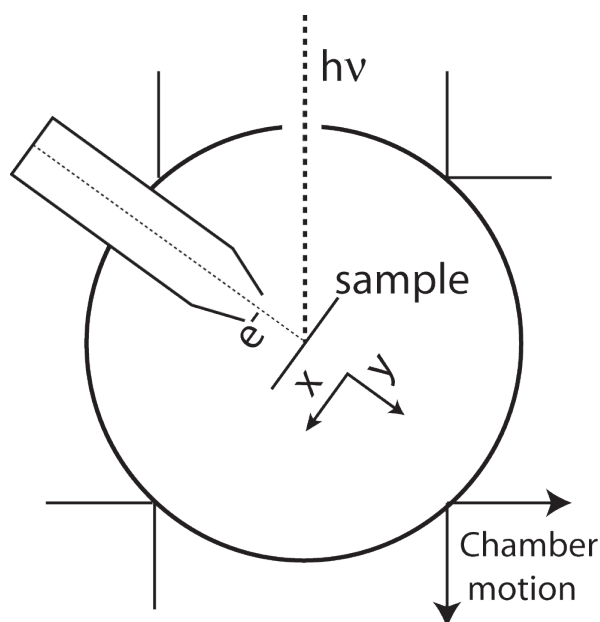

Figure 2.8: Geometrical sketch of the alignment of photon beam, sample and analyser for photoemission. The angle between the beamport and the analyser is fixed. Also the distance between analyser and sample has been optimized previously and should not be changed.

As mentioned before, the foci of the analyser and the photon beam should overlap. This means that there are three relative positions that should be fixed, within sub-millimetre limits. The ideal alignment can only be achieved by moving the entire vacuum chamber with respect to the beamline. The challenge is, therefore, to move a 1000 kg vacuum chamber with sub-millimetre precision. By equipping the chamber with four threads for height adjustment, and eight threads for left/right and front/back movement this could, however, be achieved, although improvements in terms of motorized independent movement would clearly be desirable.

The procedure followed to align the sample and chamber was as follows: the distance between the sample and analyser is fixed at 40 mm, and the sample is placed in the centre of the chamber at the level of the analyser. Using the white light (0th order) from the beamline, the chamber is then coarsely positioned to let the light impinge onto the sample for the whole angular range. The next step is to make sure that the reflection of the beam of the sample passes through the lens system and viewport of the analyser (indicated in Figure 2.4). At this point, better alignment can only be reached by actually looking at the image produced by the electrons emitted from the sample. When the band structure of the sample is not known, or not very profound because the sample needs extra treatment, a slit plate is placed at the entrance of the analyser lens. By moving the chamber in small steps in an experienced trial-and-error manner, the pattern on the screen should then look like the one presented in Figure 2.9(a). The main items to optimise are the sharpness and straightness of the lines, that they run parallel to each other, and that the centre lines are parallel to the energy axis.
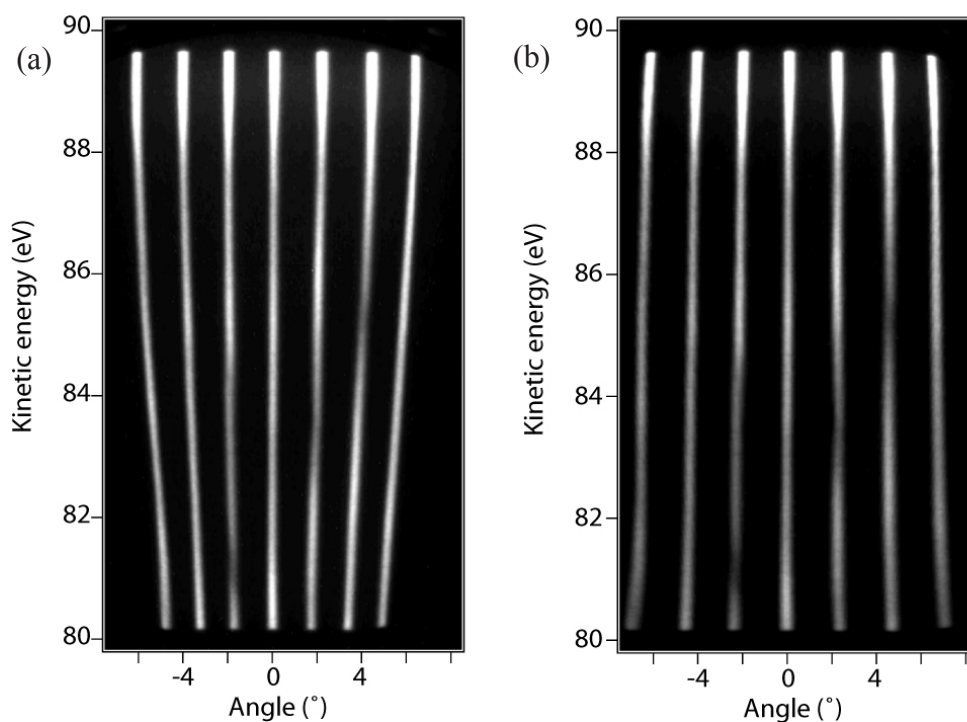

Figure 2.9: Kinetic energy vs. angle photoemission images obtained with the alignment slit plate placed in front of the analyser, before (a) and after (b) applying dispersion correction. In the alignment process, the important items to optimize in (a) are the sharpness and straightness of the lines, and their parallel arrangement. Furthermore, the centre line should be perfectly parallel to the energy axis. The slope of the lines in (a) indicates the differences in magnification factor for electrons with different kinetic energies, in (b) this difference is corrected.

When a sample with well defined sharp bands is used, as for example silicon or copper, these bands can be used as a measure for alignment without using the slit pattern. Any stray electrons should at this moment be blocked out using the iris aperture.

In the hemispherical part of the analyser, the electrons with the set kinetic energy are imaged from the entrance slit to the exit plane with magnification -1. Electrons with a lower energy are demagnified, and electrons with higher energies are magnified stronger. These chromatic aberrations result in the tilt of the lines in Figure 2.9(a). This deviation is later corrected ("dispersion correction") with software provided by the manufacturer, by using an image transformation based on a mesh warping algorithm. This algorithm was introduced for a special effect sequence in the movie "Willow" in 1988[5] and has been widely used ever since. The transformation mesh necessary for the algorithm is obtained by describing the angular dispersion relation with a seventh degree polynomial. Figure 2.9(b) shows the slit image after applying the transformation.

2.1.5 Synchrotron Radiation

For angle- and energy-resolved photoemission, a monochromatic source of photons is needed in order to make sure that electrons with the same kinetic energy originate from the same initial energy level. Synchrotron radiation is the most advanced and flexible of all possible sources, which also encompass laser (only very low photon energies), gas discharge lamps (very limited flexibility in energies) and x-ray sources (only very high energies and fixed photon energy). Synchrotron radiation is based on the fact that charged particles emit radiation when they are accelerated. A typical synchrotron facility consist of a storage ring where electrons circle with a velocity close to the speed of light, and the electrons are kept in orbit by a set of strong bending and focussing magnets. The radiation emitted by the electrons will range from the infrared to the x-ray region, which can then be monochromatized using a set of mirrors and gratings. A major advantage of the light provided by a synchrotron is that it is highly polarized, due to the fact that only the light is used that is emitted in the plane of motion of the electrons.

The experiments presented in this thesis have been performed at two different beamlines of the Berliner Speicherring-Gesellschaft für Synchrotronstrahlung (BESSY II) in Berlin-Adlershof. The first beamline that was used was also operational at BESSY I; it is the toroidal grating monochromator TGM 4 on a bending magnet. This beamline provides photons in the energy range from 8 eV to 32 eV and from 60 eV to 140 eV using two different gratings, and has as its main advantages an easy accessibility and high reliability. The second beamline is the state-of-the-art 10 m normal incidence monochromator (10mNIM) located on the U125/2 undulator. The energy range of this beamline is from 5-40 eV, with an optimal energy resolution better than 0.25 meV.

5   D.B. Smythe, ILM Technical Memo 1030, Computer Graphics Department, Lucasfilm Ltd., 1990

The combination of high intensity, variable photon energy, small spot size and well defined polarization of the synchrotron radiation with the imaging type electron energy analyser is a state-of-the-art tool for the determination of the band structure of solid state materials.

2.2 Sample preparation

2.2.1 Preparation and cleaning of the substrates

The properties of quantum well states depend strongly on the material used for the metal overlayer, because the states are derived from the bulk band of the material. The electronic and structural properties of the substrate also have a profound influence. Therefore, for a thorough study of QWS it is necessary to use several different substrates in order to gain a better understanding of all the processes involved. In this work, substrates from the three major classes of materials have been used, i.e. metals (copper), semiconductors (silicon) and semimetals (graphite), in order to determine the influence of the electronic structure of a substrate on the energies of overlayer quantum well states. For the silicon substrate, different crystal orientations and surface reconstructions were used in order to deduce the influence of the crystal structure of the substrate on the QWS.

Copper is a noble metal with a face centred cubic (*fcc*) lattice structure with an interatomic distance of 3.61 Å. In this work, the Cu(111) surface was used, which has a hexagonal atomic arrangement with a spacing of 2.56 Å between the atoms. In this orientation the electronic structure of copper shows a band gap at the zone centre with an occupied surface state. Within this gap, electron confinement in an overlayer metal is most likely to occur. Figure 2.10 shows the three-dimensional Fermi surface of copper obtained from the Fermi surface database[6], with the necks typical for the noble metals. The surface was cleaned by a combination of argon ion bombardment and annealing of the sample. Sputtering was performed at a pressure 1×10^{-5} mbar of argon with an accelerating voltage of 500 V. The crystal was annealed through a hot-plate sample holder at a temperature of around 100°C. After this treatment the cleanliness was confirmed by the presence and intensity of the surface state which is very sensitive to contamination. After deposition of foreign materials, on an initially clean substrate, a sputter and anneal cycle of less then one hour suffices to regain the clean Cu(111) surface.

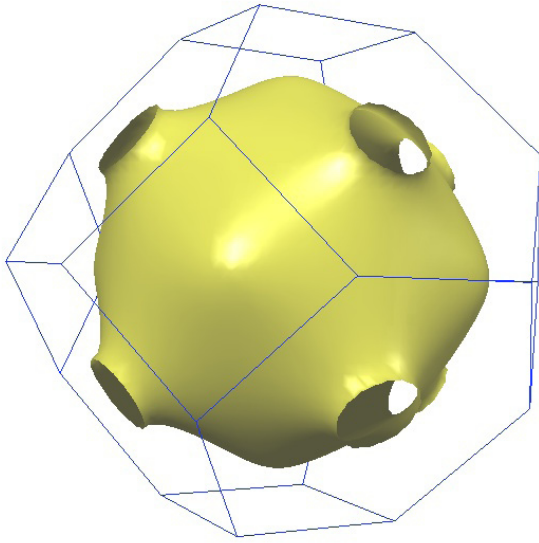6   Fermi surface database at the university of Florida http://www.phys.ufl.edu/fermisurface/

Figure 2.10: Calculated three dimensional Fermi surface of Cu. The "necks" in the (111) direction indicate the bandgap of Cu in this direction. Within this gap, electron confinement in an overlayer metal is most likely to occur. Figure from the Fermi surface database[6].

Silicon is an indirect gap semiconductor that crystallizes in the diamond structure with a lattice constant of $a = 5.43$ Å. The diamond lattice structure is based on the translation of two face centred cubic (*fcc*) structures relative to each other by a basis vector $^a/_4(1,1,1)$. Figure 2.11 shows the real space and reciprocal space of an *fcc* lattice structure. For Si(111) the direction normal to the surface is the ΓL direction and the in plane distance between the atoms is 3.13 Å. For Si(100) the normal direction is along the ΓX axis and the lattice spacing is therefore 5.43 Å. The initial step towards cleaning both surfaces is the degassing of the sample for several hours by resistive heating at a temperature of around 650°C, which can be identified by the dark red glow of the sample. To prevent the manipulator from overheating, it is either cooled by liquid nitrogen or pressurized air during this period. The Si(111) substrate is then repeatedly flashed to ~1250°C until the pressure remains below 2×10^{-9} mbar during the few seconds that the sample is at this high temperature. This procedure removes the oxide layer and results in the well known 7x7 reconstruction that can be easily confirmed by LEED. The observation of the surface states in the energy versus angle images and the sharpness of the bulk valence band features serve as a further measure of cleanliness. Si(100) can be cleaned in a similar way, whereby the flashing temperature is slightly lower and the sample should be post-annealed for several minutes at a temperature of ~600°C in order to not only create a clean but also a largely defect-free substrate. The resulting surface is a two-domain 2x1 reconstruction where the domain orientation changes by 90° on every adjacent terrace. A single domain Si(100) surface can be achieved by using samples with a 4° miscut, where after proper careful flashing and post-annealing with the current perpendicular to the miscut direction, straight terraces with double atomic steps appear. The successful formation of the single domain surface is best checked with LEED. Unless otherwise noted, all experiments on Si(100) in this thesis are on the perfectly aligned Si(100) flat substrate.
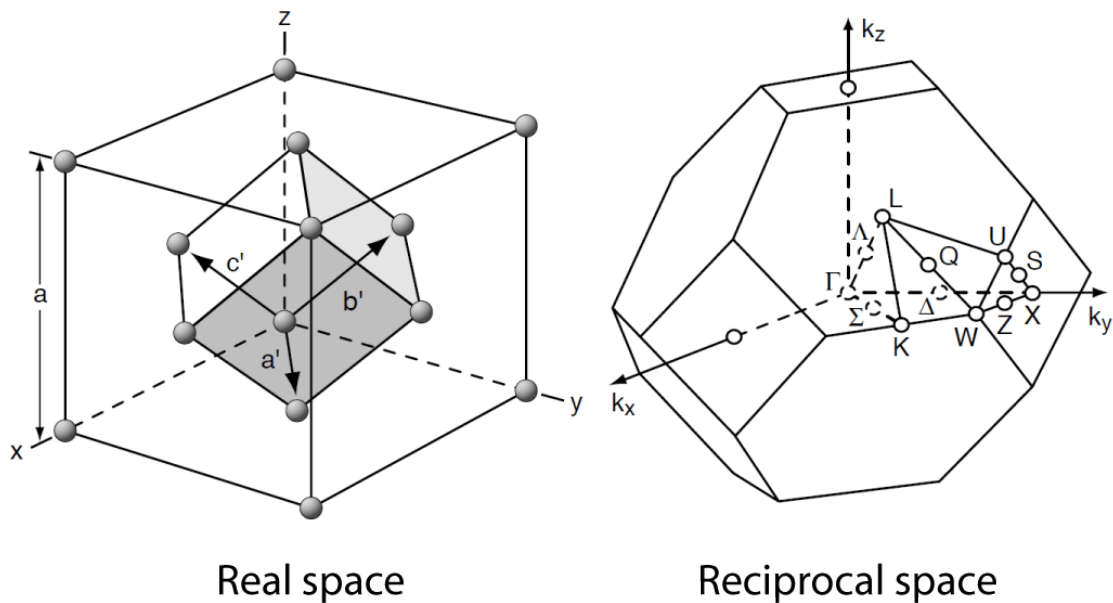
Real space   Reciprocal space

Figure 2.11: Real and reciprical space lattice structure of the face-centred cubic crystal structure. In most experiments reported in this work, the crystals are grown along the Γ-L direction in reciprocal space, corresponding to the (111) direction in real space.

A major disadvantage of the Si(111)7x7 reconstruction is that it is relatively rough on an atomic scale and therefore might limit the quality of the overlayer. To create a smoother surface, a Pb-induced √3x√3 surface reconstruction can be created[7] where the main axis of the reconstruction lattice is rotated by 30° compared to the silicon lattice. Depending on coverage, there are two different √3 phases, the high coverage α phase and the low coverage β phase. The α phase is characterized by the fact that it can be formed flat and defect free over macroscopic distances, and is therefore very well suited to serve as a template for the growth of thin metal films. This α phase is actually the most stable configuration of a whole variety of phases with similar coverage and treatment temperature, which have recently been identified by scanning tunnelling microscopy and are referred to as the "Devil's staircase"[8]. This abovementioned Pb(α) phase (henceforth referred to as the Si(111)√3 surface) can be created by low temperature deposition of 2.5 ML of Pb on the clean 7x7 surface. After deposition it still shows a 7x7 LEED pattern; this surface is then annealed to around 350°C by direct current heating, while observing the LEED pattern. At this temperature the 7x7 superstructure spots disappear and the surface is best described as Si(111)1x1-Pb. Immediate cooling back to 100 K results in the Si(111)√3 reconstruction as confirmed by LEED. Besides the atomic structure the formation of the √3 reconstruction also slightly changes the electronic structure of the substrate in that the Schottky barrier height changes from 0.70 eV to 0.93 eV[9] for the Si/Pb interface.

---

7   F. Grey *et al*, J. Phys. (Paris), **50**, 7181 (1989)

8   M. Hupalo, J. Schmalian, and M. C. Tringides, Phys. Rev. Lett. **90**, 216106 (2003)

9   D.R. Heslinga et al, Phys. Rev. Lett. **64**, 1589 (1990)
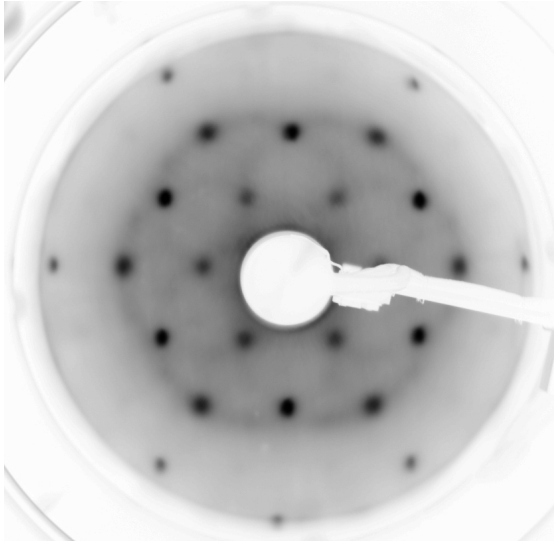
Figure 2.12: LEED pattern obtained with an electron energy of 145 eV, of hydrogen etched hexagonal 6H-SiC(0001) directly after inserting the sample in UHV without further treatment. The pattern indicates a (√3x√3)R30° surface reconstruction.

Crystalline carbon can be found in two different stable configurations: the diamond structure and the layered graphite structure. The layers in the latter structure are only weakly interacting and have a spacing of 6.71 Å. The in-plane atomic configuration is hexagonal with a lattice spacing of 2.46 Å. Mostly, highly ordered pyrolytic graphite (HOPG) is used as a substrate. For the present work, a recently developed procedure based on the formation of a graphite surface on silicon carbide[10] has been used. For this, a hexagonal 6H-SiC{0001} has been hydrogen passivated in a plasma[11] to prevent the oxidation of the surface. After insertion into UHV and without further treatment this shows a (√3x√3)R30° LEED pattern as displayed in Figure 2.12. After repeated annealing for several minutes at 1550°C all the silicon from the top layers has evaporated, and a very smooth single domain graphite sheet of several monolayers thick is created. At the centre of the Brillouin zone, this surface has no bands down to 4eV below the Fermi level, and in the ΓM direction no bands will come closer than 3eV to E_F[12]. This therefore provides an ideal substrate to study the behaviour of quantum well states in the absence of states in the underlying substrate.

2.2.2 Preparation of the metal overlayers

For the study of the formation and character of quantum well states, metals with a sp-type valence band are well suited due to the relative simplicity of their electronic structure. Aluminium has no occupied d-states and the d-bands of lead and indium are far below the Fermi level, and are core-

10   I. Forbeaux, J.-M. Themlin, J.-M. Debever, Phys. Rev. B **58**, 16396.(1998)

11   **T. Seyller, J. Phys: Cond. Matt. 16**, 1755 (2004)
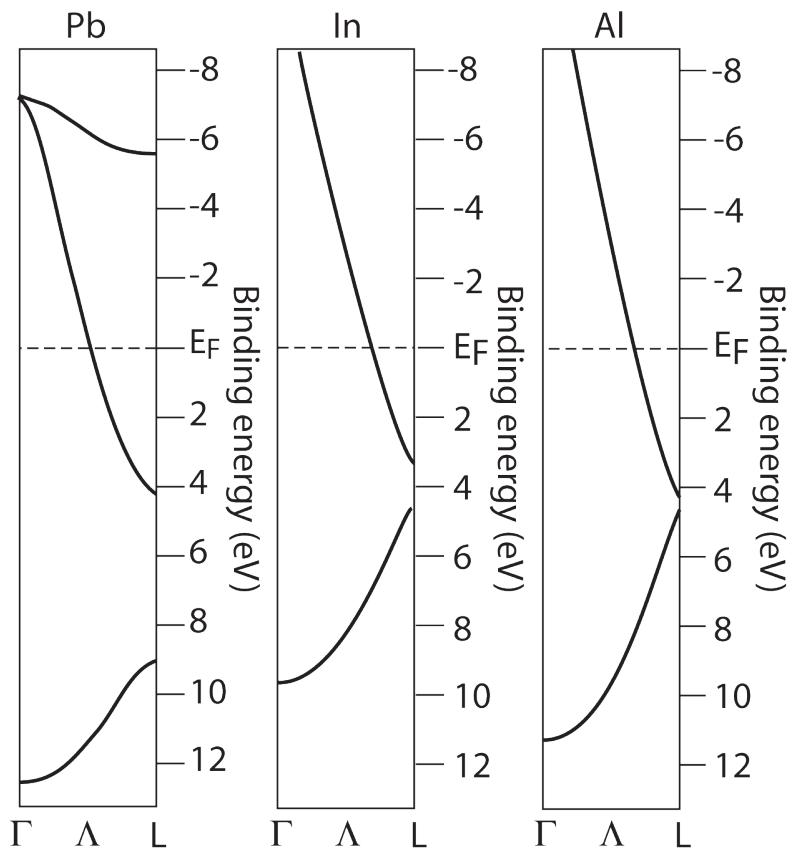
12   T. Seyller et al. Surf. Sci. in press.

Figure 2.13: Calculated band structure of Pb, In and Al along the Γ-L direction. Note the large similarities especially in the upper valence band. The point where this band crosses the Fermi level provides an indication for the number of monolayers of metal that can accommodate a new QWS.

like. These states will therefore have no relevance in this study of QWS. As can be seen in Figure 2.13, lead, indium and aluminium have a very similar upper sp-band in the Γ-L direction, which is the band that will be quantized when the films grow in the (111) direction. This makes these materials especially suitable for a comparative study of the character of QWS.

Lead crystallizes in the face centred cubic structure with a lattice constant of 4.95 Å with a real and reciprocal space as shown in Figure 2.11. The (111) surface lattice is hexagonal with an interatomic distance of approximately 2.95 Å; the inter-layer spacing is 2.86 Å. Because Pb is a very ductile material with a high atom mobility around room temperature, it is essential to evaporate the metal onto a substrate held at a temperature around 100 K in order to suppress the diffusion of the atoms. As will be shown, evaporation at this temperature results in atomically flat overlayers. As stressed in Chapter 1, QWS are derived from the bulk band structure of the material they are formed in. In Figure 2.14 angle resolved photoemission spectra for bulk Pb along the Λ direction are shown[13]. In several instances in this thesis, photoemission features resembling those in Figure 2.14 will be shown, these are then refered to as the "bulk-like feature" for Pb.

Indium has a little more complex crystal structure, namely the body-centred tetragonal (*bct*) one, with *a=b*=3.25 Å and *c*=4.94 Å. The (111) surface is therefore composed of hexagons that are compressed in one direction; an approximate average atomic distance is 2.75 Å. This structure may have a profound impact on the growth of the indium layers, as will be shown in Chapters

---

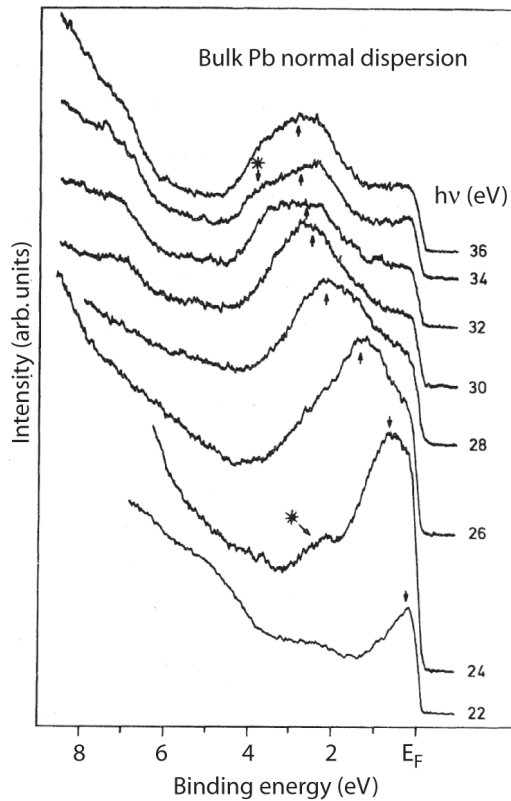13   K. Horn, B. Reihl, A. Zartner, D.E. Eastman, K. Hermann, and J. Noffke, Phys. Rev. B **30**, 1711 (1984)

Figure 2.14: Angle resolved valence level spectra for bulk Pb(111), recorded at normal emission at photon energies as indicated. Figure from Horn[13].

3 and 4. Indium shows an even stronger tendency for diffusion, hence the substrate temperature during deposition needs to be even lower than for lead. On the Si(100) substrate a temperature below 100 K suffices, but it turned out that on the Si(111) substrate the temperature needed to be below 60 K.

Aluminium was used as an overlayer material in a brief test, mainly because QWS in thin aluminium overlayers have already been extensively studied[14]. Like Pb, it has an *fcc* crystal structure with a lattice constant of 4.05 Å. Aluminium is the least prone to surface diffusion, so a deposition temperature of around 100 K was used, but it does need additional annealing around room temperature to create well-ordered layers. A major characteristic of the overlayer and substrate materials used is their relatively low reactivity with respect to the substrate materials, therefore there is absolutely no reason to assume that any of the systems will show intermixing, alloying or the formation of silicides.

14   L. Aballe, PhD Thesis, Freie Universität Berlin (2001)